







RESEARCH ARTICLE

10.1029/2023SW003695

Statistical Characteristics of Total Electron Content Intensifications on Global Ionospheric Maps

X. Meng¹ , O. P. Verkhoglyadova¹ , S. C. Chapman^{2,3,4} , N. W. Watkins^{2,5} , and M. Cafolla²

¹Jet Propulsion Laboratory, California Institute of Technology, Pasadena, CA, USA, ²Physics Department, Centre for Fusion, Space and Astrophysics, University of Warwick, Coventry, UK, ³Department of Mathematics and Statistics, University of Tromsø, Tromsø, Norway, ⁴International Space Science Institute, Bern, Switzerland, ⁵Grantham Research Institute on Climate Change and the Environment, London School of Economics and Political Science, London, UK

Key Points:

- Feature extraction software is applied to generate a total electron content (TEC) intensification data set from global TEC maps spanning 20 years
- One or two intensification(s) are identified for 86% of the TEC maps, while rest of the TEC maps have three or more intensifications
- The occurrence and strength of TEC intensifications vary with season and solar cycle, and the strength varies with geomagnetic activity

Correspondence to:

X. Meng,
xing.meng@jpl.nasa.gov

Citation:

Meng, X., Verkhoglyadova, O. P., Chapman, S. C., Watkins, N. W., & Cafolla, M. (2024). Statistical characteristics of total electron content intensifications on global ionospheric maps. *Space Weather*, 22, e2023SW003695. <https://doi.org/10.1029/2023SW003695>

Received 30 AUG 2023
Accepted 5 JAN 2024

Abstract Global ionospheric total electron content (TEC) maps exhibit TEC intensifications and depletions of various sizes and shapes. Characterizing key features on TEC maps and understanding their dynamic coupling with external drivers can significantly benefit space weather forecasting. However, comprehensive analysis of ionospheric structuring over decades of TEC maps is currently lacking due to large data volume. We develop feature extraction software based on image processing techniques to extract TEC intensification regions, that is, contiguous regions with sufficiently elevated TEC values than surrounding areas, from global TEC maps. Applying the software to the Jet Propulsion Laboratory Global Ionospheric Map data, we generate a TEC intensification data set for years 2003–2022 and carry out a statistical study on the number and strength of TEC intensifications. We find that the majority of the TEC maps (about 86%) are characterized with one or two intensification(s), while the rest of the TEC maps have three or more intensifications. Both the number and strength of TEC intensifications exhibit semi-annual variation that peaks near equinoxes and dips near solstices, as well as an annual asymmetry with larger values around December solstice compared to June solstice. The number and strength of intensifications increase with enhanced solar extreme-violet irradiance. The strength of intensifications also increases with elevated geomagnetic activity, but the number of intensifications does not. In addition, the number of intensifications is not correlated with the strength of intensifications.

Plain Language Summary The ionosphere is an upper atmospheric layer containing free electrons and ions. The abundance of ionospheric electrons varies from one location to another, creating electron intensification and depletion regions of various sizes and shapes. We develop feature extraction software to identify the electron intensification regions from two-dimensional electron abundance maps and generate a data set of their strengths and locations over two decades. We conduct a statistical study of the data set and find that most maps are with one or two intensification region(s). Maps with three or more intensification regions also occur. The number of intensification regions on a TEC map is modulated by season and solar irradiance. The strength of intensification regions is modulated by season, solar irradiance, and solar activity. Our result advances the knowledge on global ionosphere structuring, which is critical for space-borne navigation and communication.

1. Introduction

The ionospheric electron density and its height-integrated component, the total electron content (TEC), are widely used variables to describe the state of the ionosphere. In situ and remote-sensing observations have revealed comprehensive longitudinal and latitudinal variations of the ionospheric state over a range of spatial and temporal scales (Fejer, 2011; Forbes et al., 2000; Rishbeth & Mendillo, 2001), leading to a rich variety of ionospheric features. In the longitudinal and latitudinal plane, these features manifest themselves as regions of electron density or TEC enhancements and depletions with various sizes and shapes. According to their properties and driving mechanisms, the electron density enhancements and depletions are named differently. Examples include the equatorial ionization anomaly (EIA) (Appleton, 1946; Namba & Maeda, 1939), storm-enhanced density (SED) in middle-high latitudes (Foster, 1993; Foster et al., 2021), tongue of ionization in polar regions (Sato, 1959), mid-latitude ionospheric trough (Muldrew, 1965), equatorial plasma bubbles (Kil, 2015; McClure et al., 1977), and plasma blobs (Kim & Hegai, 2016; Oya et al., 1986). These enhancement and depletion structures are found to be driven and modulated by one or multiple factors including the solar irradiance, solar wind and magnetospheric conditions, geomagnetic field, neutral wind, and lower atmospheric forcing. The dynamically-changing electron

© 2024 Jet Propulsion Laboratory, California Institute of Technology and The Authors. Government sponsorship acknowledged.

This is an open access article under the terms of the [Creative Commons Attribution License](https://creativecommons.org/licenses/by/4.0/), which permits use, distribution and reproduction in any medium, provided the original work is properly cited.

density enhancements and depletions can significantly alter radio signals transmitting through the ionosphere, impacting space-borne navigation and communication (Hernandez-Pajares et al., 2011; Sparks et al., 2021).

Of all types of ionospheric electron density enhancement and depletion structures, the most significant and persistent one is the EIA. The classical picture of the EIA is characterized by two electron density enhancement regions separated by the geomagnetic equator with an electron density depletion region in-between. The so-called two-peak EIA has been extensively observed and investigated over decades, leading to a good understanding of the EIA formation (Balan et al., 2018), morphology (e.g., Andreeva et al., 2000; Eastes et al., 2019; Immel et al., 2006; Khadka et al., 2018; Li et al., 2021; J. Liu et al., 2020; Loutfi et al., 2022; Luan et al., 2015; Nigussie et al., 2022; Sagawa et al., 2005; Walker, 1981), temporal variability (e.g., Y. Chen et al., 2016; Y. N. Huang & Cheng, 1996; C. H. Lin, Hsiao, et al., 2007; C. H. Lin, Liu, et al., 2007; H.-F. Tsai et al., 2001; T. C. Tsai et al., 2019; Yeh et al., 2001; Yue et al., 2015), and its response to geomagnetic storms and lunar phase (e.g., J. Y. Liu et al., 2013; Luan, 2021; Mannucci et al., 2005; Mendillo, 2006; Padatella & Forbes, 2010; Wu et al., 2020). Deviations from the classical two-peak EIA have also been reported. Specifically, a significant amount of single-peak EIA events have been observed with TEC data along a certain longitude (L. Huang et al., 2014) and in situ electron density measurements (Fathy & Ghamry, 2017; Hussien et al., 2023). The single peaks could be manifestations of strong asymmetry in northern and southern EIA crests, which are caused by weakened equatorial plasma fountain and the neutral wind crossing the equator (Fathy & Ghamry, 2017; L. Huang et al., 2014). Three or four peaks in the latitudinal distribution of the electron density or TEC have been identified under both geomagnetic quiet and disturbed conditions (Astafyeva et al., 2016, 2017; Cai et al., 2020, 2022; Horvath & Lovell, 2010; Jiang et al., 2020; Lei et al., 2015; C. S. Lin et al., 2022; Maruyama et al., 2016; Rajesh et al., 2016; Xiong et al., 2019). The formation of the extra peak(s) has been attributed to several mechanisms. For instance, during intense geomagnetic storms, SED structure (Coster et al., 2016) could extend from high latitudes to middle latitudes to form extra ionization peaks poleward of the two-peak EIA. During geomagnetic quiet time and depending on the local time when the extra ionization peaks appear, possible causes of the extra peaks include meridional neutral winds (Maruyama et al., 2016), the combined effect of $E \times B$ drift, neutral winds, and ionosphere-plasmasphere plasma flow (Rajesh et al., 2016), plasma diffusive flux (Jiang et al., 2020), and the latitudinal variation of $E \times B$ drift (Cai et al., 2022).

The existence of EIA-like features with a single latitudinal peak and three or more latitudinal peaks implies comprehensive underlying ionospheric processes beyond those responsible for the classical two-peak EIA features. Our knowledge on the characterization and formation of large-scale ionospheric structuring is far from complete. In particular, due to observational constraints, the majority of existing studies do not simultaneously reveal the longitudinal, latitudinal, and temporal variations of ionospheric features on a global scale. This information can be provided by time-dependent longitudinal-latitudinal maps of ionospheric electron density or relevant physical parameters that cover either the entire globe or a significant portion of the globe. Different types of global-scale longitudinal-latitudinal maps have been utilized to investigate EIAs or EIA-like features. Examples include climatological maps of the F2-layer peak electron density obtained from a global collection of ionospheric radio occultation measurements (e.g., Tulasi Ram et al., 2009; Yue et al., 2015), global TEC maps constructed from Global Navigation Satellite System (GNSS) ground-based measurements (e.g., Verkhoglyadova et al., 2021), and more recently, OI 135.6 nm emission maps for the nighttime ionosphere from Global-scale Observations of the Limb and Disk (GOLD) imager (Cai et al., 2023; Eastes et al., 2019). These studies offer valuable global-scale characterization of EIAs and EIA-like features. Nevertheless, long-term statistics of large-scale ionospheric features, EIA included, are rarely extracted from global-scale longitudinal-latitudinal maps. This is partially due to the difficulty in identifying desired patterns consistently from a vast amount of two-dimensional maps.

Recently, image processing techniques and machine-learning-based algorithms have been applied to recognize patterns from ionospheric TEC maps or to complete ionospheric TEC maps (Z. Chen et al., 2019; Starr et al., 2022; Sun et al., 2023; Verkhoglyadova et al., 2021, 2022). Motivated by these powerful approaches and their promising performance, we develop feature extraction software based on an image processing library and the prior work of Verkhoglyadova et al. (2021) to automatically identify intensification regions in global ionospheric TEC maps. The software is then utilized to generate a data set of large-scale TEC intensifications (with a spatial scale greater than 800 km) from global TEC maps over 20 years. The identified TEC intensifications include TEC enhancement regions of EIAs and EIA-like features. We use this data set of large-scale TEC intensifications to determine how the properties of TEC intensifications statistically correlate with season, solar

cycle, and geomagnetic activity. Our study offers new perspective to the characterization and understanding of large-scale ionospheric structuring.

2. Methodology

2.1. Global Ionospheric Map Data Used in the Study

Global Ionospheric Maps (GIMs) are global ionospheric TEC maps generated from GNSS TEC measurements using ground-based receivers worldwide (e.g., Hernandez-Pajares et al., 2017; Roma-Dollase et al., 2018). Several GIM data products of various spatial and temporal resolutions have been generated at Jet Propulsion Laboratory (JPL) (Mannucci et al., 1998). This study uses the most recently updated JPL GIM data product JPLD, which provides global TEC maps from year 2003 to year 2022 at a spatial resolution of 1° by 1° and a temporal resolution of 15 min (https://sideshow.jpl.nasa.gov/pub/iono_daily/gim_for_research/jpld/). The number and distribution of GNSS ground-based receivers from which measurements are collected to generate the JPLD data product evolves over time: about 200 receivers prior to 2019 and about 300 receivers or more subsequently. The total available JPLD global TEC maps during 2003–2022 number about 0.7 million, so that manual identification of TEC intensifications is not feasible. In addition, manual identification may introduce subjective biases. Therefore, these global TEC maps are input into feature extraction software for an automatic extraction of TEC intensifications and obtain TEC intensification data set for 2003–2022.

2.2. Feature Extraction Software

The TEC feature extraction software is built upon the labeling script reported in Verkhoglyadova et al. (2021). The previous work utilized several methods from OpenCV's image processing library (<https://opencv.org/>) to recognize boundaries of high density TEC regions (HDRs), that is, TEC enhancement regions, that meet the defined criteria. The labeling script counts and outputs the number of HDRs for each given TEC map. The script is used to determine the number of HDRs for approximately 10,000 TEC maps selected from 10 years of the JPL GIM data. The occurrence of different HDR counts and its variation with solar cycle phase, season, and geomagnetic activity are examined (Verkhoglyadova et al., 2021, 2022). For this work, we have modified and improved the labeling script to construct the feature extraction software.

The workflow of the feature extraction software consists of five major steps: (a) For a given TEC map gridded in longitude and latitude, the software computes the Laplacian value using the Laplacian operator from OpenCV for each grid point. The Laplacian operator (∇^2) calculates the second-order derivative of the TEC to identify edges of TEC intensification regions. The TEC map is then processed with a Laplacian threshold and filtered with a TEC threshold. (b) The software applies Dilate and Erode operators from OpenCV on the remaining grid points and cleans noises on the image with medianBlur operator to obtain an image with intensification regions only. (c) The software identifies individual objects from the image and produces a statistics output for each object using Connected Components operator from OpenCV. (d) The sizes of the objects and their possible intersections are examined, so the objects are kept as, merged into, or removed from identified TEC intensifications. Merging of objects occurs when they wrap around the east and west edges of a map. Removal of objects occurs when their sizes fall below a size threshold. (e) The number of TEC intensifications and characteristics of each intensification on the given TEC map are collected as outputs of the software.

Apart from gridded TEC maps, the input to the feature extraction software also includes three adjustable parameters:

- **TEC threshold**, in percentile of all TEC values on a given TEC map. The TEC threshold value can vary from map to map. Grid points with TEC values below the value that corresponds to the TEC threshold are excluded from being identified as intensification regions. This sets a lower threshold for the intensity of any possible intensifications to be identified and can exclude faint TEC intensifications.
- **Laplacian threshold**, typically at a value between -1 and 0 . Grid points with Laplacian values greater than the Laplacian threshold are excluded from being identified as intensification regions. The Laplacian threshold provides a cut-off for the sharpness of the edges of possible intensification regions, thus identified intensifications have a sufficiently large contrast with their surrounding areas in terms of the TEC values.
- **Size threshold**, in number of grid cells. The size threshold defines the minimum size of intensification regions. Intensifications covering a smaller number of grid cells than the size threshold are discarded from the final intensifications identified. The size threshold restricts the spatial scale of the TEC intensifications identified.

2.3. TEC Intensification Data Set

We apply the feature extraction software to JPLD global TEC maps for years 2003–2022. A parameter sensitivity study is first conducted to determine the input threshold values optimized for extracting large-scale intensifications from the global TEC maps. The Laplacian threshold is fixed to be 0, which defines the edge of an intensification region at where the local TEC gradient maximizes. TEC threshold values between the 90th and 97th percentiles are tested for a randomly selected subset of TEC maps from the 20 years of data. Threshold values between the 95th and 97th percentiles do not significantly change the number of TEC intensifications identified. Threshold values below the 95th percentile lead to less TEC intensifications with larger sizes compared to thresholds of 95th–97th percentiles, such that the software identifies two-peak EIA features as single intensifications for many maps. We also experiment with size threshold values between 50 and 100 grid cells, which do not impact the result much. Therefore, optimal parameters are identified as follows. The TEC threshold is the 97th percentile, which corresponds to a different TEC value for each TEC map, accommodating the variation in the overall level of ionospheric background TEC under different space weather conditions, in particular for different strengths of solar extreme-violet (EUV) irradiance driving. The Laplacian threshold is 0. The size threshold is 65 grid cells, corresponding to 0.1% of the total number of grid cells on the TEC map of 1° by 1° resolution. This also defines the minimum spatial scale of the identified large-scale intensification to be at least 800 km. With these optimal threshold values, the software is able to recognize TEC intensification regions from EIAs and EIA-like features, providing both longitudinal and latitudinal structure information for the TEC intensifications.

The resulting TEC intensification data set consists of the number and characteristics of all TEC intensifications identified for every JPLD TEC map during 2003–2022. For each TEC intensification, the data set includes the following characteristics: the maximum, median, and minimum TEC within the intensification region, the geographic longitude and latitude of the TEC maximum, the regional electron content (REC) of the intensification, the size of the intensification, and the number of GNSS receivers located within and nearby the intensification region. The REC is calculated as the summation of the multiplication of the TEC value and its corresponding grid cell area for all grid cells falling into an intensification region: $REC = \sum_{i,j} TEC_{ij} S_{ij}$, where i and j are longitudinal and latitudinal grid indices for the grid cells inside of the intensification region. TEC_{ij} is the TEC value of grid cell (i, j) , and S_{ij} is the area of grid cell (i, j) . The REC is defined similarly to the global electron content (GEC) that sums over global grid cells (Afraimovich et al., 2006, 2008). The unit of REC is GECU and $1 \text{ GECU} = 10^{32}$ electrons. The REC indicates the overall strength of an intensification.

Figure 1 displays examples of TEC intensifications found by the feature extraction software. Four TEC maps at different times during a geomagnetically disturbed day, 7 December 2022, are shown, with one, two, three, and four intensifications identified respectively. Identified intensification regions are bounded by thick gray curves. The intensification regions with black stars, which mark the locations of local TEC maxima within the intensifications, are written into the TEC intensification data set. Intensifications smaller than the size threshold, for instance the small intensification near 60°E0°N/S in Figure 1d, are excluded from the data set. Figure 1b is a representative case of the classical two-crest EIA feature being identified as two separated intensifications on the TEC map, while Figures 1a, 1c, and 1d illustrate the additional variety in intensification morphology. Note that the latitudinal TEC distribution along some longitudinal sectors would still display two peaks in the one-, three-, and four-intensification cases shown in Figures 1a, 1c, and 1d. This distinguishes our TEC intensifications from the latitudinal TEC or electron density peaks along certain longitudes investigated by many previous studies (e.g., Astafyeva et al., 2016; Fathy & Ghamry, 2017; L. Huang et al., 2014; Nigussie et al., 2022).

3. Results

In this study, we focus on analyzing the number and strength of TEC intensifications. The strength of intensifications is calculated as the sum of the REC from all intensifications identified on a given map: Total REC = $\sum_{n=1}^N REC_n$, where N is the number of all intensifications in the map and n is the index of each intensification. Thus, two time series are obtained: the number of TEC intensifications and the total REC of TEC intensifications per 15 min map. Both time series are at 15 min temporal resolution and span the years 2003–2022 inclusive. The properties of the two time series are displayed in Figure 2. Figure 2a displays a histogram of the number of intensifications for all TEC intensifications from 2003 to 2022. The exact map counts for different numbers of intensifications are given in Table 1. According to Figure 2a and Table 1, most TEC maps are characterized by a single intensification or two intensifications. The occurrence of one-intensification and two-intensification

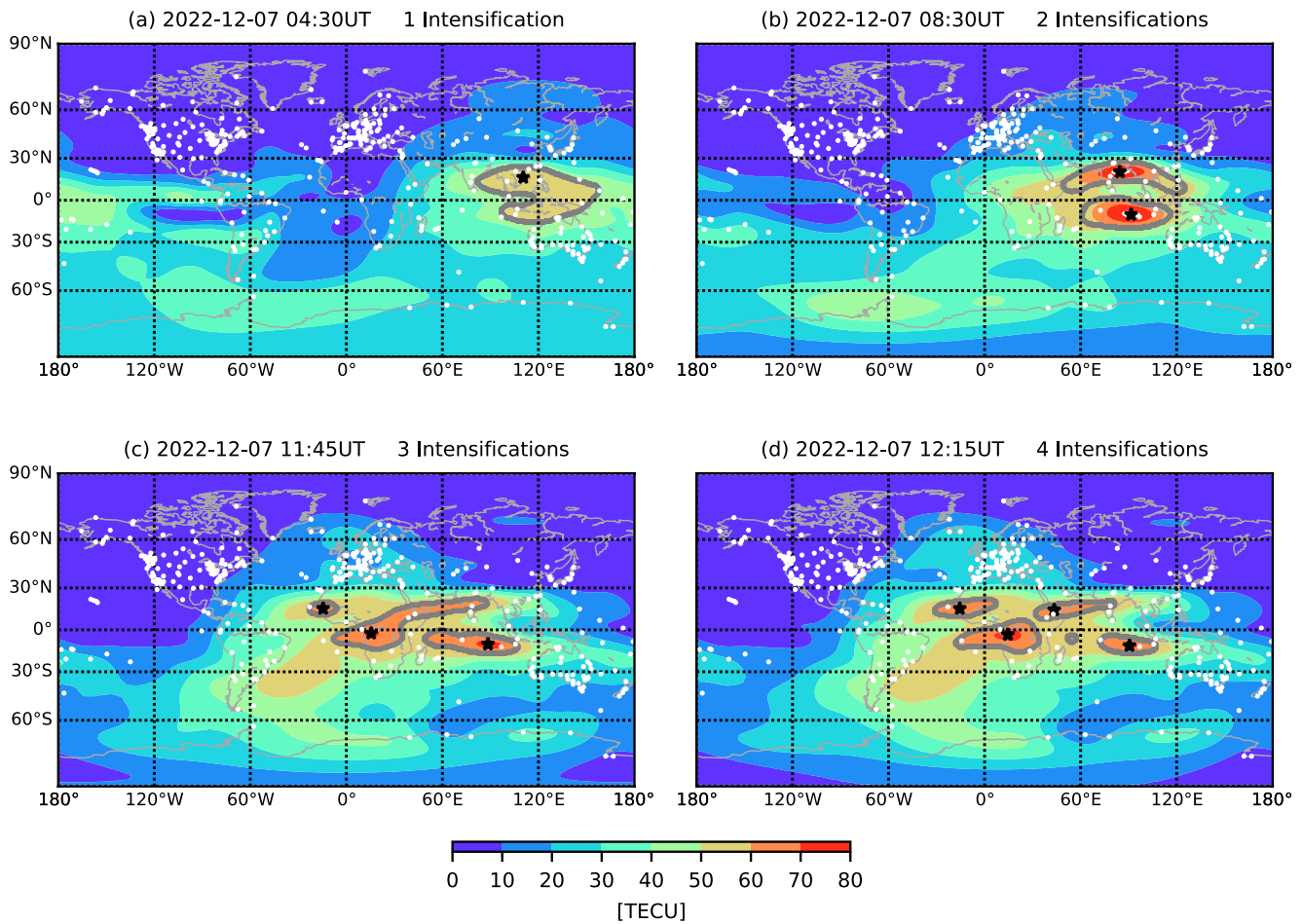


Figure 1. Example total electron content (TEC) maps with (a) one, (b) two, (c) three, and (d) four intensifications identified. The thick gray curve bounds an intensification region, while the black star marks the location of the maximum TEC within the intensification. White dots represent Global Navigation Satellite System ground-based receivers used for producing the map.

cases are comparable and together constitute 86.5% of all maps. A significant occurrence of TEC maps with three intensifications are found as well and constitute 11.7% of all maps. The remaining less than 2% maps are identified with four, five, or six intensifications. Shown in Figure 2b, the value for the total REC varies from less than 0.05 GECU to 0.25 GECU with a peak around 0.06 GECU. Figure 2c plots the daily maximum and daily average values for the number of intensifications as a function of time. The daily maximum number of intensifications is between two and five most of the time and can reach six occasionally, while the daily average number of intensifications varies between one and three over the two decades. The daily averaged total REC, shown in Figure 2d, exhibits a clear correspondence with the solar cycle of activity, represented by the monthly average sunspot number.

3.1. Number of TEC Intensifications

Inspired by the apparent semi-annual variations of the total REC shown in Figure 2d, a natural question to ask is whether the number of intensifications contains any semi-annual or other seasonal variabilities. To investigate this, we obtain the average for each month of the year of the number of TEC intensifications in each 15-min-resolution map, with the averages being taken over all years in 2003–2022 inclusive. The result is shown in Figure 3a, where the black line plots the average for each month, and the upper and lower bounds of the gray-shaded area are respectively the maximum and minimum number of intensifications seen in each month, over all years 2003–2022. The plot shows a clear semi-annual variation, with more intensifications seen near equinoxes than near solstices. Furthermore, we divide the series of intensifications into four seasonal subsets: northern hemisphere (NH) spring

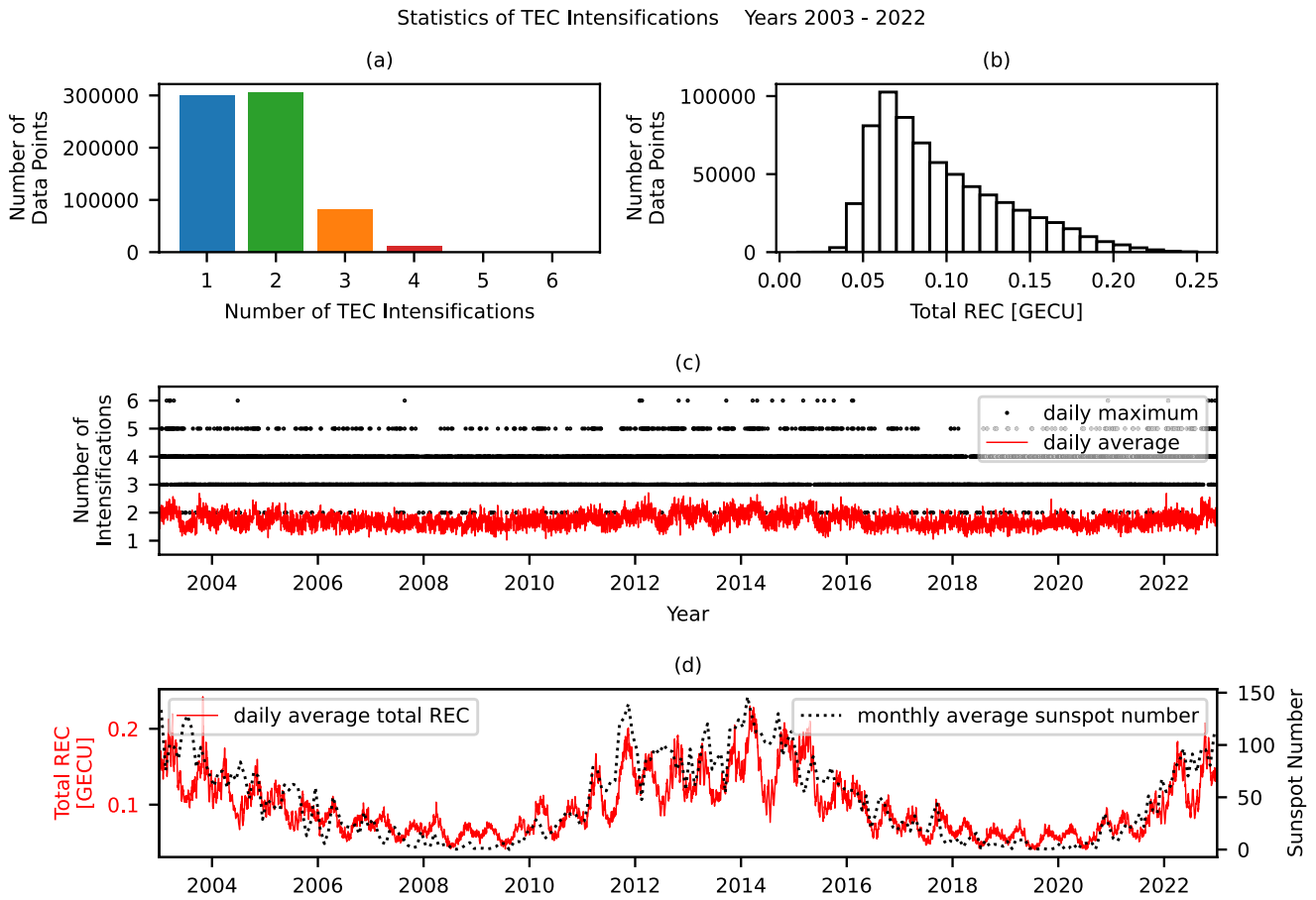


Figure 2. (a) Histogram of the number of intensifications per 15 min from years 2003 to 2022. The number of data points is equivalent to the number of total electron content (TEC) maps. (b) Histogram of the total regional electron content (REC) of intensifications, representing the strength of all intensifications identified on a TEC map, for years 2003–2022. (c) Time series of the daily maximum and daily average numbers of TEC intensifications. (d) Time series of the daily average total REC. The black dotted line represents the monthly average sunspot number.

for data in March, April, and May; NH summer for data in June, July, and August; NH fall for data in September, October, and November; NH winter for data in December, January, and February. The occurrence of different numbers of intensifications per map in each season is visualized in Figure 3b. The colors distinguish data from different subsets/seasons. The bar values for fall and winter are plotted as negative to facilitate comparison among four seasons. In addition, we estimate the uncertainty as $\pm \sqrt{M}$ on M counts to add the error bar for each bin. For most bins, the uncertainty is within $\pm 1\%$ of the bin value, thus the error bars are tiny in Figure 3b. For all seasons except NH summer, two-intensification case is slightly more frequently occurring than one-intensification case.

Quantitatively, the counts for two-intensification case are 13%, 7%, and 25% more than one-intensification case respectively for spring, fall, and winter. For NH summer, however, one-intensification case is 37% more frequently occurring than two-intensification case. In fact, among the four seasons, NH summer contributes the largest to all one-intensification case counts. For TEC maps identified with a single intensification region, they have a higher chance (30%) to occur in NH summer than spring (24%), fall (24%), and winter (22%).

We now consider variation with the solar cycle of activity by testing for ordering of the number of intensifications with the intensity of solar EUV irradiance. The daily F10.7 index is adopted as a proxy for the solar EUV irradiance. Figure 4a shows how the F10.7 values are categorized into three levels: low (≤ 80 SFU), middle (>80 SFU and <130 SFU), and high (≥ 130

Table 1
Total Electron Content Map Counts for Various Numbers of Intensifications From 2003 to 2022

Cases	Counts	Counts/Total counts (%)
One-intensification	300,165	42.8
Two-intensification	306,414	43.7
Three-intensification	81,909	11.7
Four-intensification	11,789	1.7
Five-intensification	867	0.1
Six-intensification	40	0.006

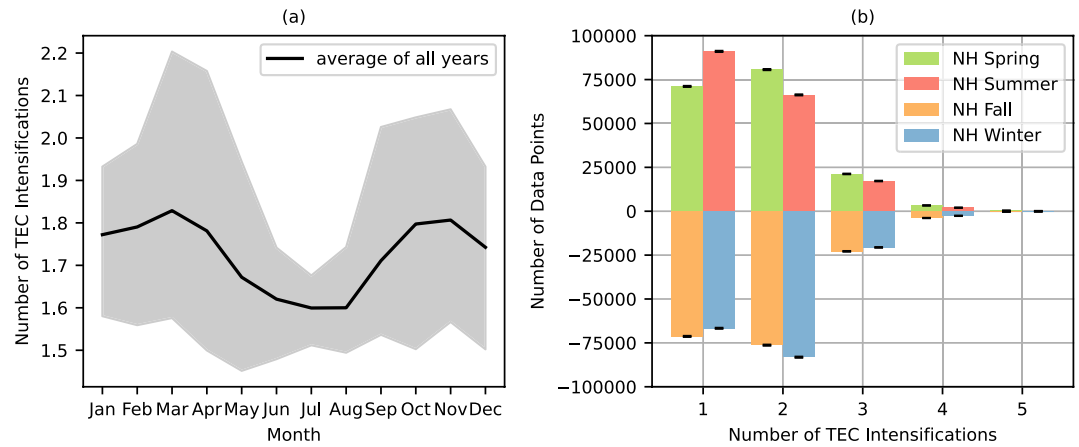


Figure 3. (a) Monthly averaged number of total electron content (TEC) intensifications. The gray-shaded area is the spread of the monthly averages for individual years during 2003–2022, and the black curve is the mean of all 20 years for the monthly averages. (b) Histograms of the number of TEC intensifications for northern hemisphere spring (March–May), summer (June–August), fall (September–November), and winter (December–February), for all data during 2003–2022. The black error bars are computed as $\pm \sqrt{M}$ on M counts for individual bins.

SFU), indicated by gray, light purple and dark purple respectively. The thresholds for the three F10.7 levels are chosen such that the time interval for the low level covers a few years around a solar minimum, and the time interval for the high level covers a few years around a solar maximum. To be consistent with the temporal resolution of

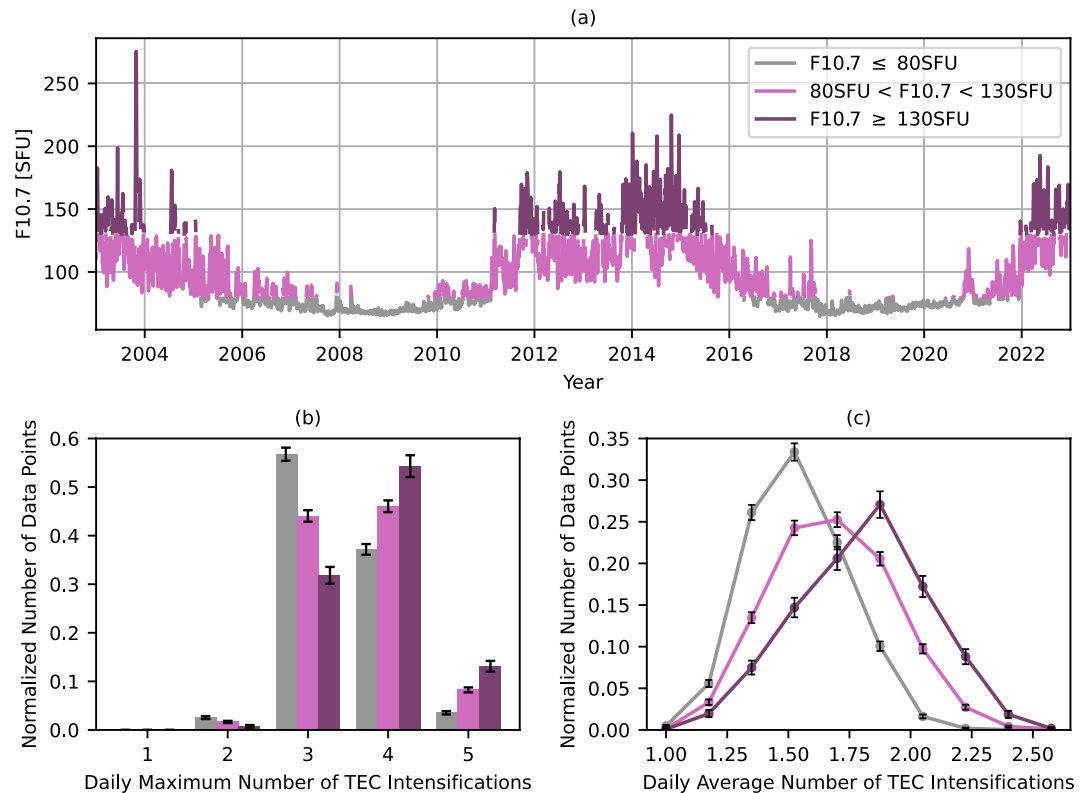


Figure 4. (a) The daily F10.7 index during 2003–2022, categorized into three levels marked by different colors. (b) Normalized histograms of the daily maximum number of total electron content (TEC) intensifications for three different F10.7 levels color-coded as in (a). (c) Normalized histograms of the daily average number of TEC intensifications for three different F10.7 levels color-coded as in (a). Histogram values are plotted as dots with connected straight lines. For (b) and (c), the data for different F10.7 levels are normalized separately. The black error bars are computed in the same way as for Figure 3b then normalized.

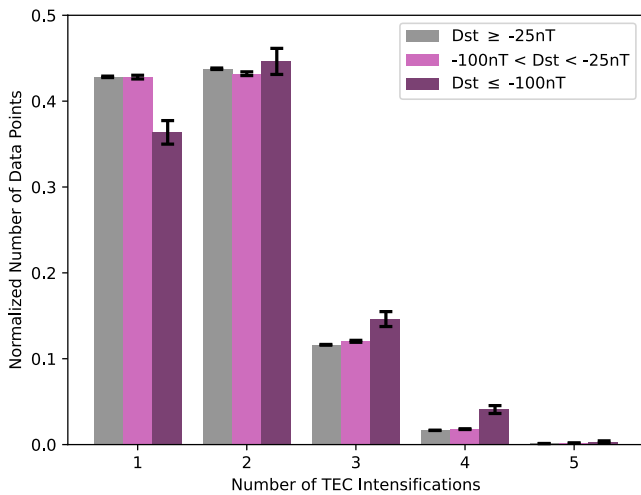


Figure 5. Normalized histograms of the number of total electron content (TEC) intensifications for three different geomagnetic activity levels based on the Dst index. The histograms are normalized separately for different Dst levels. The black error bars are computed in the same way as for Figure 3b then normalized.

F10.7, we use the daily maximum and daily average number of TEC intensifications and categorize the intensification data by the three F10.7 levels. The histograms of the daily maximum and daily average number of TEC intensifications that occur during different F10.7 levels are displayed in Figure 4b as a bar graph and (c) as a line graph respectively. In (c), the histogram values are plotted as colored dots connected with straight lines. Note that for panels (b) and (c), the histograms are normalized for each F10.7 level, therefore the values of all same-colored data points add to 1. The normalization eliminates potential bias introduced by different number of data points for different categories. The error bars are computed using the same method as for those in Figure 3b and then normalized along with the data. The daily maximum number of intensifications peaks at 3 for the low F10.7 level and peaks at four for middle and high F10.7 levels. The daily average number of intensifications exhibits a similar shift toward the larger daily average number of intensifications under higher F10.7 levels, peaking at 1.5, 1.75, and 2 respectively for low, middle, and high F10.7 levels. In particular, cases when the daily average number of intensifications equal to/greater than 2 nearly always occur under middle and high F10.7 levels. The variability with the F10.7 reveals the non-negligible impact of the solar EUV irradiance on the number of TEC intensifications per map.

As the morphology of EIAs and EIA-like features can change significantly during geomagnetic storms, we investigate the possible relation between the number of intensifications and geomagnetic activity. The Dst index is used as a proxy for the level of geomagnetic activity. According to the value of Dst, three levels of geomagnetic activity are defined: $Dst \geq -25$ nT for no or little geomagnetic activity, -100 nT $< Dst < -25$ nT for weak and moderate geomagnetic storms, and $Dst \leq -100$ nT for intense geomagnetic storms. The 15-min-resolution data, that is, number of intensifications per map, is then categorized into three subsets corresponding to the three levels of geomagnetic activity. As Dst is an hourly index, we assume that a Dst value is representative for the entire hour, and thus the categorization is based on the date and hour each 15-min-resolution data point falls into. The result is displayed in Figure 5, in which different colors represent different subsets of data. The histograms are normalized for each subset of data, so the heights of all same-colored bars add to 1. During $Dst \geq -25$ nT, the chances for a TEC map featured with one, two, three, and four intensifications are 43%, 44%, 12%, and 2%, respectively. During -100 nT $< Dst < -25$ nT, the chances for a TEC map featured with one, two, three, and four intensifications are 43%, 43%, 12%, and 2%, respectively. During $Dst \leq -100$ nT, the chances for a TEC map featured with one, two, three, and four intensifications become 36%, 45%, 15%, and 4%, respectively. Therefore, the data subsets during $Dst \geq -25$ nT and -100 nT $< Dst < -25$ nT have nearly identical histograms across various number of intensifications, while for $Dst \leq -100$ nT, the histogram is slightly shifted toward higher numbers of TEC intensifications. The similarity and difference among the histograms of the three data subsets indicate that geomagnetic activity has minimal impact on the number of TEC intensifications, though intense geomagnetic activity can result in more TEC intensifications appearing on a map.

3.2. Strength of TEC Intensifications

For the strength of TEC intensifications represented by the 15-min-resolution total REC data, we take a similar approach as used above (to analyze the number of TEC intensifications) to investigate its variations with seasons, solar EUV irradiance, and geomagnetic activity. The seasonal variability of the total REC is shown in Figure 6, in the same format as Figure 3. The semi-annual variation of the total REC can be clearly seen in Figure 6a, where the black line plots the average for each month, and the upper and lower bounds of the gray-shaded area are respectively the maximum, and minimum number of intensifications seen in each month, over all years 2003–2022. The trend is similar to that seen in Figure 3a. The total REC peaks in March–April and October–November, and dips in January–December and June–July. Classifying the total REC data by season, in the same manner as for the number of intensifications above, gives the histograms shown in Figure 6b. The error bars are tiny, as the uncertainty is within $\pm 2\%$ of the bin value for most bins. We again flip the vertical axis for the NH fall and winter, for a better contrast among the four seasons. The histograms indicate very similar total REC

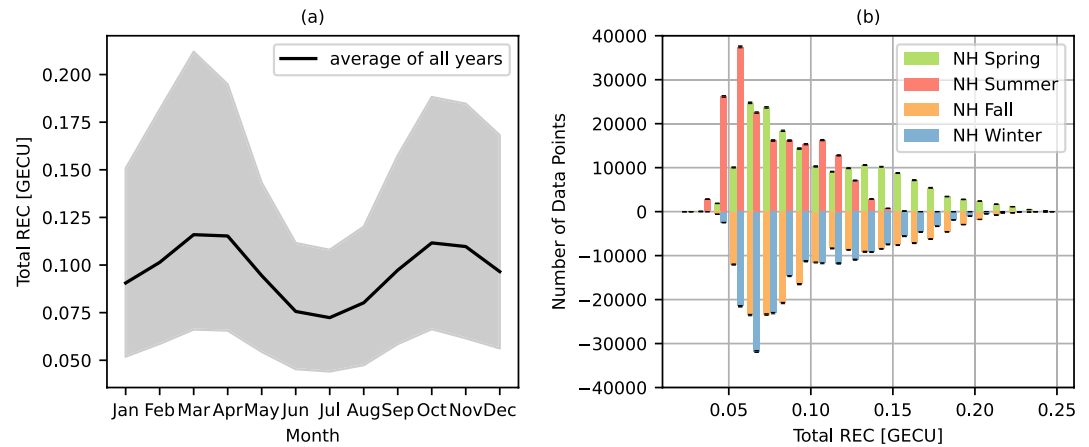


Figure 6. (a) Monthly averaged total regional electron content (REC). The gray-shaded area is the spread of the monthly averages for individual years during 2003–2022, and the black curve is the mean of all 20 years for the monthly averages. (b) Histograms of the total REC for northern hemisphere spring (March–May), summer (June–August), fall (September–November), and winter (December–February), for all data during 2003–2022. The black error bars are computed in the same way as for Figure 3b.

distributions during NH spring and fall, as well as a somewhat narrower distribution during NH winter, which has less data points at larger total REC values during the winter than during the spring and fall. The histogram for NH summer does not show the extended tail seen in the other seasons, with nearly no summer data points beyond 0.15 GECU. To emphasize this, approximately 47%, 46%, and 40% of data points in spring, fall, and winter respectively are greater than 0.1 GECU, compared to 23% of data points in summer. The summer histogram also peaks at a smaller total REC value (0.05–0.06 GECU) than the histograms for other three seasons (0.06–0.07 GECU). The smaller total REC values during NH summer compared to NH winter agrees with the smaller spread of the total REC in June–August than December–February in Figure 6a. This result implies stronger TEC intensifications during NH winter than NH summer.

The variation of the total REC with the solar EUV irradiance is displayed in Figure 7. As in the analysis for the number of intensifications, the F10.7 index is used to represent the intensity of the solar EUV irradiance and divide the total REC data into three subsets corresponding to three different F10.7 levels. We calculate the daily maximum and daily average of the total REC and investigate their histograms under different F10.7 levels. The histograms are obtained by binning the data every 0.01 GECU and normalizing the values so that all values add

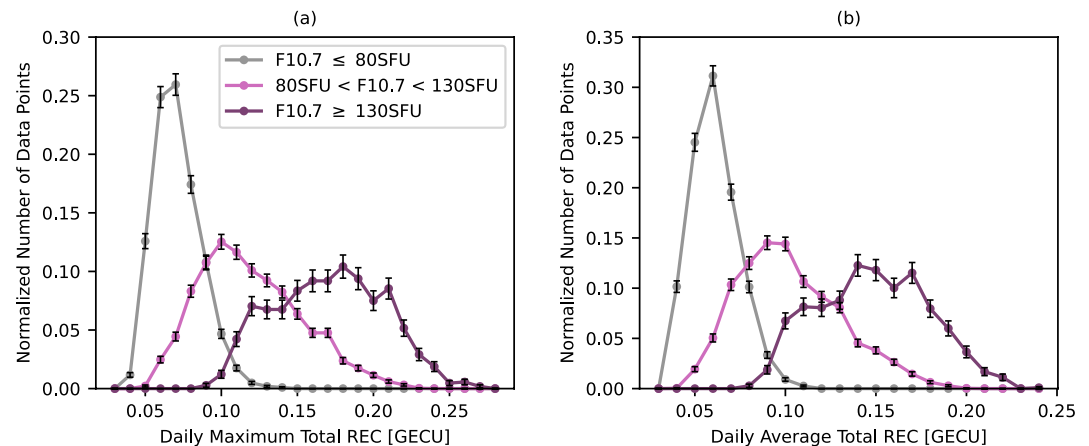


Figure 7. (a) Normalized histograms of the daily maximum total regional electron content (REC) for three different F10.7 levels. (b) Normalized histograms of the daily average total REC for three different F10.7 levels. The histograms are normalized separately for different F10.7 levels and displayed as line-connected dots with error bars. The error bars are computed in the same way as for Figure 3b then normalized.

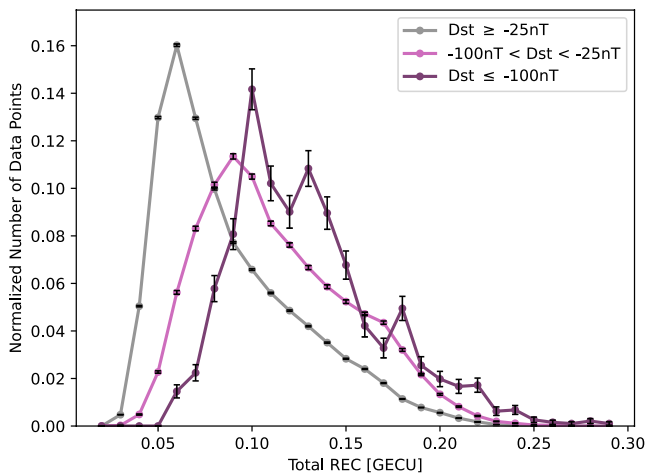


Figure 8. Normalized histograms of the total regional electron content for three different geomagnetic activity levels based on the Dst index. The histograms are normalized separately for different Dst levels and are plotted as line-connected dots with error bars. The error bars are computed in the same way as for Figure 3b then normalized.

to 1 for each F10.7 level. The normalized histogram values are plotted as dots connected with straight lines. The histogram of the daily maximum total REC peaks at 0.07–0.08 GECU, 0.1–0.11 GECU, 0.18–0.19 GECU respectively for low, middle, and high F10.7 levels. The histogram of the daily average total REC peaks at 0.06–0.07 GECU, 0.09–0.1 GECU, 0.14–0.15 GECU respectively for low, middle, and high F10.7 levels. The histograms show a very distinctive trend: the higher the F10.7, the larger the total REC. In other words, the TEC intensifications are stronger under higher F10.7. In addition, the histograms are broader for the high F10.7 level than the low F10.7 level, indicating a larger spread of the total REC values during solar maxima than during solar minima.

Figure 8 visualizes the relationship between the total REC and the strength of geomagnetic activity. The data is classified using the same three levels of Dst in the above analysis for the number of intensifications versus geomagnetic activity. The data is binned every 0.01 GECU to obtain histogram values, which are then normalized so all values sum up to 1 for each Dst level. The normalized histogram values are plotted as dots connected with lines. From Figure 8, the histograms of the total REC under the three different Dst levels are clearly different, unlike the similar histograms of the number of intensifications shown in Figure 5. The histogram maxima are at 0.06–0.07 GECU, 0.09–0.1 GECU, 0.1–0.11 GECU respectively for $Dst \geq -25$ nT,

$-100 \text{ nT} < Dst < -25 \text{ nT}$, and $Dst \leq -100 \text{ nT}$. For $Dst \geq -25$ nT, about 35% of data points are with the total REC above 0.1 GECU. For $-100 \text{ nT} < Dst < -25 \text{ nT}$, about 62% of data points have the total REC above 0.1 GECU. For $Dst \leq -100 \text{ nT}$, about 68% of data points have the total REC above 0.1 GECU. Essentially, with a lower Dst level, the histogram shifts toward larger total REC values and peaks at a larger total REC. Thus, geomagnetic activity can significantly affect the strength of the TEC intensifications. Higher levels of geomagnetic activity typically correspond to stronger TEC intensifications.

3.3. Relationship Between the Number and Strength of TEC Intensifications

Both the number and strength are important characteristics of TEC intensifications identified from the global TEC maps. Recall that the strength of TEC intensifications is defined as the total REC from all intensifications, regardless of how many intensification regions there are, on a given TEC map. Does a TEC map with more intensification regions have a larger total REC? Motivated by this question, we investigate the relationship between the number and strength of intensifications.

Figure 9a displays the histogram of the total REC for each case of one, two, three, and four intensifications, indicated by different colors. Five- or six-intensification cases are not considered as they are rare (see Table 1). The histograms are binned every 0.005 GECU and the histogram bin values are plotted as colored curves. The uncertainty is estimated as before using $\pm \sqrt{M}$ on M counts, and plot the uncertainty as color-shaded area around each histogram curve. The shaded areas are nearly invisible in Figure 9a, as most of the uncertainties are within 2% of the corresponding histogram bin value for one-, two-, and three-intensification cases and within 6% for four-intensification case. Despite their different number of data points, all histograms shown in Figure 9a peak around similar total REC values 0.06–0.07 GECU. The width of the histograms are also similar. The similarities of the histograms to each other indicate that the number of intensifications does not have a clear correlation with the total REC. TEC maps with more intensification regions do not typically correspond to larger total REC values. In addition, the outstanding tail population of the two-intensification case is particularly interesting. Taking into account the slightly more two-intensification maps than one-intensification maps (Table 1) and comparing the histograms of one-intensification and two-intensification cases, the more tail population above 0.11 GECU in the two-intensification histogram compensates for the lower peak total REC between 0.06 and 0.07 GECU in the two-intensification histogram. A better view of the tail population for not only the two-intensification case, but also three- and four-intensification cases is shown in Figure 9b, which displays the probability density of the total REC, also binned every 0.005 GECU, and uncertainties in color-shaded areas around the probability density curves. All two-, three-, and four-intensification cases exhibit a larger tail population above 0.11 GECU

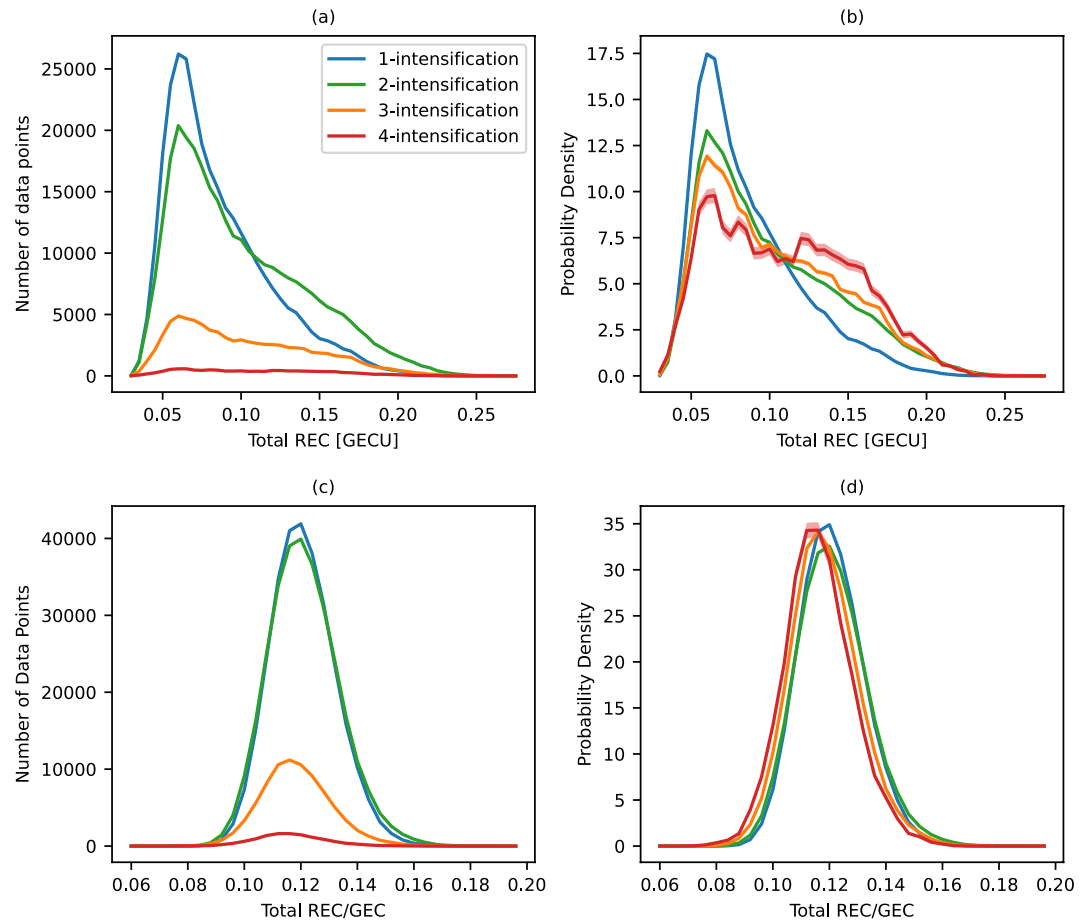


Figure 9. (a) Histograms of the total regional electron content (REC) for different numbers of intensifications for all data during years 2003–2022. Colors represent different cases for the number of intensifications. (b) Probability density of the total REC for different numbers of intensifications for all data during years 2003–2022. For each number of intensification represented by a colored curve, the area under the curve is one. (c) Same as (a) but for the relative strength of intensifications, which is defined as the ratio between the total REC and global electron content (GEC). (d) Same as (b) but for the relative strength of intensifications. In all four panels, the uncertainties, estimated as for Figure 3b, are plotted as color-shaded areas around the curves.

than the one-intensification case. For one-intensification, the population above 0.11 GECU covers 23% of all one-intensification maps, while for two-, three-, and four-intensification, the tail population above 0.11 GECU is 37%, 40%, 49% of their respective total amount of maps. The different tail population for different number of intensifications indicates that the TEC maps with more-than-one intensifications are 14%–26% more likely to have larger total REC values than the TEC maps with a single intensification. However, the most probable total REC value (0.06–0.07 GECU) at the peak of the probability density is independent of the number of intensifications.

The strength of TEC intensifications naturally varies with the background TEC over the globe. Specifically, on TEC maps with elevated TEC values globally, the TEC within intensification regions are larger as well. For further investigation on the relationship between the number and strength of intensifications, we define the relative strength of TEC intensifications, the relative total REC, as the ratio between the total REC and the GEC for a given TEC map. The relative total REC is indicative of the ratio between the electron content within intensification regions and the electron content globally, providing a quantitative measure of the intensification strength with the impact of the background TEC variations excluded. The histograms and probability densities of the relative total REC are shown in Figures 9c and 9d, respectively. The bin size is 0.004 for both the histograms and probability densities. The uncertainties are plotted as color-shaded areas around the histogram and probability density curves. Comparing to the histograms of the total REC shown in Figure 9a, the histograms of the relative

total REC no longer show enhanced tail populations for two-, three-, and four-intensification cases. Moreover, the probability density curves of one-, two-, three-, and four-intensification cases are strikingly similar as shown in Figure 9d. The nearly identical probability density curves indicate little to no relationship between the number of intensifications and the relative strength of intensifications. Therefore, without considering the background TEC, the total strength of all intensifications on a TEC map, that is, the relative REC, does not depend on how many intensification regions there are on the TEC map.

4. Discussion

4.1. Variations With Season, Solar Cycle, and Geomagnetic Activity

Both the number and strength of TEC intensifications exhibit seasonal variability similar to the extensively-studied semi-annual and annual variations of the ionospheric F2-layer peak electron density and TEC (e.g., Croom et al., 1960; Kawamura et al., 2002; Mendillo et al., 2005; Rishbeth, 1998; Torr & Torr, 1973; Yonezawa, 1959). Both the semi-annual and annual variations are observed globally. The semi-annual variation refers to larger electron density or TEC around equinoxes than around solstices, while the annual variation, also known as the annual asymmetry, refers to larger electron density or TEC around December solstice than around the June solstice. The physical mechanism driving the semi-annual and annual variations is not fully understood, however several possible factors have been identified. Factors leading to the semi-annual variation include Earth's obliquity, mesopause turbulent mixing, and lower atmospheric gravity wave and tidal mixing (Jones et al., 2018; Qian et al., 2013). For the annual asymmetry, possible causes include the offset of the geomagnetic center from the geographic center, different Sun-Earth distances at December and June solstices, mesopause turbulent mixing, and lower atmospheric tidal forcing (Dang et al., 2017; Qian et al., 2013; Zeng et al., 2008). Both the semi-annual variation and annual asymmetry are seen in the total REC of TEC intensifications (Figure 6). As the semi-annual variation and annual asymmetry of ionospheric electron density and TEC are global phenomena, the TEC within intensification regions can naturally exhibit the same variation patterns. Recall that the total REC takes into account the TEC values inside intensification regions and the sizes of intensification regions, it is reasonable for the total REC to inherit the semi-annual/annual variation patterns from the TEC. More interestingly, the semi-annual variation and annual asymmetry are found in the number of TEC intensifications (Figure 3). This provides new insight to the known semi-annual/annual variations of the ionosphere: These variations manifest in global ionospheric structuring as well. Further research is needed to determine the cause of the semi-annual/annual variations in the number of TEC intensifications, and whether the physical mechanism behind is the same mechanism responsible for the semi-annual/annual variations in the electron density and TEC.

Variations with the solar cycle are also present in the number and strength of TEC intensifications. Specifically, we find clear relationships between the number of TEC intensifications and the F10.7 index, as well as between the total REC and the F10.7, shown in Figures 4 and 7. Both the number of intensifications and the total REC tend to increase with increasing F10.7 values. The trend is particularly strong for the total REC. The variation of the total REC with the F10.7 is expected as the ionospheric electron density is modulated by the solar EUV irradiance. Stronger solar EUV irradiance typically leads to more daytime ionospheric electrons via photoionization. Our result agrees with previous findings reporting globally enhanced ionospheric electron density or TEC with an increasing F10.7 until saturation is reached at very high F10.7 values (e.g., Afraimovich et al., 2008; Balan et al., 1994; L. Liu et al., 2006). The variation of the number of TEC intensifications with the F10.7 indicates the modulation of the solar EUV irradiance on the global ionospheric structure. Specifically, photochemical processes influence the occurrence of the intensifications. Although our definition of TEC intensifications is different from the latitudinal electron density/TEC peaks studied previously, they still share some synergy as most of our 1-intensification scenarios correspond to latitudinally single peaks. We could compare our result with previous results on the occurrence of single-peak events with solar EUV flux. L. Huang et al. (2014) reports that single-peak TEC events around 120°E longitude preferably occur on days with low solar EUV flux. Hussien et al. (2023) finds that the number of single-peak events in the electron density data from SWARM increases with increasing F10.7. Our result shows that one-intensification case occurs more often with lower F10.7 values than higher F10.7 values, supporting the conclusion of L. Huang et al. (2014).

The strength of TEC intensifications is found here to vary strongly with geomagnetic activity whereas number of TEC intensifications varies only weakly with geomagnetic activity. For the strength of TEC intensifications, the total REC tends to be larger during geomagnetic storm times than during quiet times, and it tends to

increase with decreasing Dst values. This suggests that the TEC intensification regions experience positive storm effects (Buonsanto, 1999). The intensity of the positive storm effects scales with the strength of geomagnetic storms. We have not considered possible time delays between the total REC response and the progression of geomagnetic storms (Immel & Mannucci, 2013), which would be interesting to explore in future research. For the number of TEC intensifications, its relation with the intensity of geomagnetic activity is weak. In particular, for one-intensification case, its occurrence is slightly reduced during intense geomagnetic storms with $Dst \leq -100$ nT than during weak/moderate storms and quiet times. This is different from the previous finding of enhanced occurrences of electron density single-peaks with increasing geomagnetic activity by Hussien et al. (2023), although they used Kp instead of Dst as the indicator for the geomagnetic activity level. According to our results, the number of intensifications has a small tendency to increase when geomagnetic activity becomes more intense, which might be caused by SED structures during intense geomagnetic storms being identified as TEC intensifications. In addition, our results show fairly frequent occurrences of three-intensification case and four-intensification case even during geomagnetic quiet times, which implies that the classical two-peak EIA structure does not always hold for the quiet-time ionosphere. This supplements the result of Astafyeva et al. (2016) that latitudinal three-peak electron density structures occur often during geomagnetic quiet times.

4.2. Uncertainties of the Statistical Study

Our statistical study contains uncertainties that could impact the accuracy of the reported results. First, the study relies on the TEC intensification data set generated with the TEC feature extraction software. The robustness of the software in pattern recognition has been demonstrated via visually inspecting the identified TEC intensification regions for ten thousands of TEC maps randomly selected (Verkhoglyadova et al., 2021). The software can successfully recognize TEC intensification regions of various shapes over a vast majority of the TEC maps. In this work we have introduced three adjustable parameters to the software: the TEC, Laplacian, and size thresholds, in order to better control the effectiveness and robustness of the software. Our parameter sensitivity experiment helps determine the optimal values of the TEC and size thresholds, with Laplacian threshold value fixed at 0, for extracting TEC intensifications out of JPLD TEC maps. The zero Laplacian threshold determines the edge of a TEC intensification along the local maxima of TEC gradient surrounding the intensification region. Nevertheless, the Laplacian threshold can take a non-zero value, which would define the edge of an intensification region differently from the zero Laplacian threshold. With various choices of the Laplacian threshold value, optimal values of the TEC and size thresholds vary as well. In fact, different choices of three parameter value combinations can lead to intensification regions of somewhat different sizes and shapes, and even different number of intensifications identified from a map. The parameter values and the identified TEC intensification regions are related in a subtle manner, requiring further investigation. For a more complete study in the future, one could generate a statistically significant amount of parameter value combinations for input to the feature extraction software and estimate the uncertainty of the intensification extraction for every TEC map. The resulted uncertainty-bounded intensification characteristics can be added to the TEC intensification data set.

Second, the study utilizes one of the JPL GIM data products, the JPLD TEC maps, for years from 2003 to 2022. While GIMs offer global TEC data continuously over decades, their accuracy heavily depends on the distribution of GNSS ground-based receivers. As the JPL GIM relies on interpolating GNSS TEC measurements to generate TEC data on a global grid, the TEC data in regions with a poor coverage of receivers is more smoothed out than the TEC data in regions with abundant receivers. Therefore, the identified TEC intensifications are conservative, since intensifications could be missed due to lack of TEC measurement (Verkhoglyadova et al., 2021). The TEC intensification data set records the number of GNSS ground-based receivers within and surrounding each identified intensification region. About 90% of the intensifications in the data set have at least one receiver within or surrounding them, while 75% intensifications have at least two receivers. Hence, most of the intensifications in the data set investigated by the statistical study are with fairly reliable TEC data.

5. Conclusions

Motivated by the knowledge gap in large-scale ionospheric structuring, especially EIA-like features with single, three, or more latitudinal electron density peak(s), we carry out a statistical study to characterize TEC intensification regions on global ionospheric TEC maps spanning 20 years. In the study, TEC feature extraction software has been developed to identify elevated TEC regions on gridded TEC maps. Utilizing the software, a TEC

intensification data set is generated from the $1^\circ \times 1^\circ \times 15$ min JPL GIM of two decades from 2003 to 2022. For each global TEC map, the data set records the number and characteristics of all TEC intensifications with spatial scales of 800 km and above. For each TEC intensification, its characteristics includes the maximum, median, and minimum TEC within the intensification, the geographic location of the TEC maximum, the REC and the size of the intensification, as well as the number of GNSS ground-based receivers within and surrounding the intensification region. We then focus on the number and total REC of the intensifications from the data set to investigate the statistical behavior of the number and strength of the TEC intensifications. The main findings are:

- 86.5% of the global TEC maps during 2003–2022 are characterized with one or two TEC intensification(s), with a slightly higher chance of two intensifications. 11.7% of the TEC maps are identified with three intensifications, while the rest 2% TEC maps are with four to six intensifications.
- Both the number and strength of TEC intensifications exhibit semi-annual and annual variations similar to the semi-annual variation and annual asymmetry observed previously in the ionospheric electron density and TEC. Specifically, the number and strength of intensifications are larger around equinoxes than around solstices, and they are larger around December solstice than around June solstice.
- The number and strength of TEC intensifications also vary with the solar EUV irradiance, proxied by F10.7. A higher F10.7 level corresponds to more intensifications and, in particular, stronger intensifications on a TEC map.
- The strength of TEC intensifications increases with enhanced geomagnetic activity indicated by the Dst index, while the number of TEC intensifications does not clearly relate to the level of geomagnetic activity except that it can slightly increase during intense geomagnetic storms with $Dst \leq -100$ nT.
- A TEC map with more intensifications identified does not necessarily have a higher total REC, indicating little to no relationship between the number and strength of TEC intensifications.

Our results provide characterization of the large-scale TEC intensifications that could manifest themselves not only as two-peak EIAs but also as EIA-like structures with a single peak or three-or-more peaks. Deviations from the classical two-peak EIA structure are common even during geomagnetic quiet times, implying the complexity of the global ionospheric structure. For the first time, we show that the number of TEC intensifications per map exhibits semi-annual/annual variations and modulation from the solar EUV irradiance. The work contributes to the knowledge of global ionospheric structuring and variability, as well as potentially benefits ionospheric TEC forecasting. In addition, the 20-year TEC intensification data set offers valuable long-term data for ionospheric structures. Future work remains as to investigate other intensification characteristics from the data set, for instance the geographic location and size. With additional observational data and modeling, case studies can also be conducted for specific one-intensification and three-or-more-intensification events selected from the data set, in order to understand the formation of these intensifications.

Data Availability Statement

The monthly average sunspot number is taken from <https://www.sidc.be/SILSO/datafiles>. The F10.7 index is obtained from https://lasp.colorado.edu/lisird/data/cls_radio_flux_f107/. The Dst index is from <https://wdc.kugi.kyoto-u.ac.jp/dstdir/index.html>. The JPL GIM data product JPLD is available at https://sideshow.jpl.nasa.gov/pub/iono_daily/gim_for_research/jpld/. The TEC intensification data set generated in the study can be found at Meng and Verkhoglyadova (2023).

Acknowledgments

The research was carried out at the Jet Propulsion Laboratory, California Institute of Technology, under a contract with NASA. Sponsorship of NASA ROSES Living With a Star Tools and Methods Program (NNH21ZDA001N-LWSTM) is gratefully acknowledged. The OpenCV team is gratefully acknowledged as well (<https://opencv.org/>). SCC acknowledges support from ISSI via the J. Geiss fellowship. SCC, NWW, and MC acknowledge AFOSR Grant FA8655-22-1-7056. XM and OPV would like to thank A. J. Mannucci (JPL) for insightful discussions.

References

- Afraimovich, E. L., Astafeyeva, E. I., Oinats, A. V., Yasukevich, Y. V., & Zhivetiev, I. V. (2008). Global electron content: A new conception to track solar activity. *Annales Geophysicae*, 26(2), 335–344. <https://doi.org/10.5194/angeo-26-335-2008>
- Afraimovich, E. L., Astafeyeva, E. I., & Zhivetiev, I. V. (2006). Solar activity and global electron content. *Doklady Earth Sciences*, 409A(6), 921–924. <https://doi.org/10.1134/s1028334x06060195>
- Andreeva, E. S., Franke, S. J., Yeh, K. C., & Kunitsyn, V. E. (2000). Some features of the equatorial anomaly revealed by ionospheric tomography. *Geophysical Research Letters*, 27(16), 2465–2468. <https://doi.org/10.1029/1999gl003725>
- Appleton, E. V. (1946). Two anomalies in the ionosphere. *Nature*, 157(3995), 691. <https://doi.org/10.1038/157691a0>
- Astafeyeva, E., Zakharenkova, I., & Huba, J. D. (2017). Three-peak ionospheric equatorial ionization anomaly: Development, drivers, statistics. In *Proceedings of the 14th ionospheric effects symposium*.
- Astafeyeva, E., Zakharenkova, I., & Pineau, Y. (2016). Occurrence of the dayside three-peak density structure in the F2 and the topside ionosphere. *Journal of Geophysical Research: Space Physics*, 121(7), 6936–6949. <https://doi.org/10.1002/2016JA022641>
- Balan, N., Bailey, G. J., Jenkins, B., Rao, P. B., & Moffett, R. J. (1994). Variations of ionospheric ionization and related solar fluxes during an intense solar cycle. *Journal of Geophysical Research*, 99(A2), 2243–2253. <https://doi.org/10.1029/93JA02099>

- Balan, N., Souza, J., & Bailey, G. J. (2018). Recent developments in the understanding of equatorial ionization anomaly: A review. *Journal of Atmospheric and Solar-Terrestrial Physics*, 171, 3–11. <https://doi.org/10.1016/j.jastp.2017.06.020>
- Buonsanto, M. J. (1999). Ionospheric storms — A review. *Space Science Reviews*, 88(3/4), 563–601. <https://doi.org/10.1023/A:1005107532631>
- Cai, X., Burns, A. G., Wang, W., Coster, A., Qian, L., Liu, J., et al. (2020). Comparison of GOLD nighttime measurements with total electron content: Preliminary results. *Journal of Geophysical Research: Space Physics*, 125(9), e2019JA027767. <https://doi.org/10.1029/2019JA027767>
- Cai, X., Qian, L., Wang, W., McInerney, J. M., Liu, H.-L., & Eastes, R. W. (2022). Investigation of the post-sunset extra electron density peak poleward of the equatorial ionization anomaly southern crest. *Journal of Geophysical Research: Space Physics*, 127(10), e2022JA030755. <https://doi.org/10.1029/2022JA030755>
- Cai, X., Wang, W., Eastes, R. W., Qian, L., Pedatella, N. M., Aa, E., et al. (2023). Quatorial ionization anomaly discontinuity observed by GOLD, COSMIC-2, and ground-based GPS receivers' network. *Geophysical Research Letters*, 50(10), e2023GL102994. <https://doi.org/10.1029/2023GL102994>
- Chen, Y., Liu, L., Le, H., Wan, W., & Zhang, H. (2016). Equatorial ionization anomaly in the low-latitude topside ionosphere: Local time evolution and longitudinal difference. *Journal of Geophysical Research: Space Physics*, 121(7), 7166–7182. <https://doi.org/10.1002/2016JA022394>
- Chen, Z., Jin, M., Deng, Y., Wnag, J., Huang, H., Deng, X., & Huang, C.-M. (2019). Improvement of a deep learning algorithm for total electron content maps: Image completion. *Journal of Geophysical Research: Space Physics*, 124(1), 790–800. <https://doi.org/10.1029/2018ja026167>
- Coster, A. J., Erickson, P. J., Foster, J. C., Thomas, E. G., Ruohoniemi, J. M., & Baker, J. B. H. (2016). Solar cycle 24 observations of storm enhanced density and the tongue of ionization. In T. Fuller-Rowell, E. Yizengaw, P. H. Doherty, & S. Basu (Eds.), *Ionospheric space weather: Longitude and hemispheric dependencies and their solar, geomagnetic, and lower atmosphere connections*. John Wiley.
- Croom, S. A., Robbins, A. R., & Thomas, J. O. (1960). Variation of electron density in the ionosphere with magnetic dip. *Nature*, 185(4717), 902–903. <https://doi.org/10.1038/185902a0>
- Dang, T., Wang, W., Burns, A., Dou, X., Wan, W., & Lei, J. (2017). Simulations of the ionospheric annual asymmetry: Sun-Earth distance effect. *Journal of Geophysical Research: Space Physics*, 122(6), 6727–6736. <https://doi.org/10.1002/2017JA024188>
- Eastes, R. W., Solomon, S. C., Daniell, R. E., Anderson, D. N., Burns, A. G., England, S. L., et al. (2019). Global-scale observations of the equatorial ionization anomaly. *Geophysical Research Letters*, 46(16), 9318–9326. <https://doi.org/10.1029/2019GL084199>
- Fathy, A., & Ghamry, E. (2017). A statistical study of single crest phenomenon in the equatorial ionospheric anomaly region using Swarm A satellite. *Advances in Space Research*, 59(6), 1539–1547. <https://doi.org/10.1016/j.asr.2016.12.020>
- Fejer, B. G. (2011). Low latitude ionospheric electrodynamics. *Space Science Reviews*, 158(1), 145–166. <https://doi.org/10.1007/s11214-010-9690-7>
- Forbes, J., Palo, S., & Zhang, X. (2000). Variability of the ionosphere. *Journal of Atmospheric and Solar-Terrestrial Physics*, 64(8), 685–693. [https://doi.org/10.1016/s1364-6826\(00\)00029-8](https://doi.org/10.1016/s1364-6826(00)00029-8)
- Foster, J. C. (1993). Storm time plasma transport at middle and high latitudes. *Journal of Geophysical Research*, 98(A2), 1675–1689. <https://doi.org/10.1029/92ja02032>
- Foster, J. C., Zou, S., Heelis, R. A., & Erickson, P. J. (2021). Ionospheric storm-enhanced density plumes. In G. Huang, G. Lu, Y. Zhang, & L. J. Paxton (Eds.), *Ionosphere dynamics and applications*. <https://doi.org/10.1002/9781119815617.ch6>
- Hernandez-Pajares, M., Juan, J. M., Sanz, J., Aragon-Angel, A., Garcia-Rigo, A., Salazar, D., & Escudero, M. (2011). The ionosphere: Effects, GPS modeling and the benefits for space geodetic techniques. *Journal of Geodesy*, 85(12), 887–907. <https://doi.org/10.1007/s00190-011-0508-5>
- Hernandez-Pajares, M., Roma-Dollase, D., Krankowski, A., Garcia-Rigo, A., & Orus-Perez, R. (2017). Methodology and consistency of slant and vertical assessments for ionospheric electron content models. *Journal of Geodesy*, 91(12), 1405–1414. <https://doi.org/10.1007/s00190-017-1032-z>
- Horvath, I., & Lovell, B. C. (2010). Storm-enhanced plasma density (SED) features investigated during the Bastille Day superstorm. *Journal of Geophysical Research*, 115(A6), A06305. <https://doi.org/10.1029/2009JA014674>
- Huang, L., Wang, J., Jiang, Y., Huang, J., Chen, Z., & Zhao, K. (2014). A preliminary study of the single crest phenomenon in total electron content (TEC) in the equatorial anomaly region around 120°E longitude between 1999 and 2012. *Advances in Space Research*, 54(11), 2200–2207. <https://doi.org/10.1016/j.asr.2014.08.021>
- Huang, Y. N., & Cheng, K. (1996). Solar cycle variations of the equatorial ionospheric anomaly in total electron content in the Asian region. *Journal of Geophysical Research*, 101(A11), 24513–24520. <https://doi.org/10.1029/96ja01297>
- Hussien, F., Ghamry, E., Mohammed, Y., & Fathy, A. (2023). Ionospheric single crest events at different altitudes and activity levels observed by Swarm constellation. *Astrophysics and Space Science*, 368(4), 25. <https://doi.org/10.1007/s10509-023-04178-2>
- Immel, T. J., & Mannucci, A. J. (2013). Ionospheric redistribution during geomagnetic storms. *Journal of Geophysical Research: Space Physics*, 118(12), 7928–7939. <https://doi.org/10.1002/2013JA018919>
- Immel, T. J., Sagawa, E., England, S. L., Henderson, S. B., Hagan, M. E., Mende, S. B., et al. (2006). Control of equatorial ionospheric morphology by atmospheric tides. *Geophysical Research Letters*, 33(15), L15108. <https://doi.org/10.1029/2006GL026161>
- Jiang, C., Wang, W., Yang, G., Liu, J., & Zhao, Z. (2020). An investigation of mid-latitude ionospheric peak in TEC using the TIEGCM. *Journal of Atmospheric and Solar-Terrestrial Physics*, 211, 105480. <https://doi.org/10.1016/j.jastp.2020.105480>
- Jones, M., Emmert, J. T., Drob, D. P., Picone, J. M., & Meier, R. R. (2018). Origins of the thermosphere-ionosphere semiannual oscillation: Reformulating the “thermospheric spoon” mechanism. *Journal of Geophysical Research: Space Physics*, 123(1), 931–954. <https://doi.org/10.1002/2017JA024861>
- Kawamura, S., Balan, N., Otsuka, Y., & Fukao, S. (2002). Annual and semiannual variations of the midlatitude ionosphere under low solar activity. *Journal of Geophysical Research*, 107(A8), SIA 8-1–SIA 8-10. <https://doi.org/10.1029/2001JA000267>
- Khadka, S. M., Valladares, C. E., Sheehan, R., & Gerrard, A. J. (2018). Effects of electric field and neutral wind on the asymmetry of equatorial ionization anomaly. *Radio Science*, 53(5), 683–697. <https://doi.org/10.1029/2017RS006428>
- Kil, H. (2015). The morphology of equatorial plasma bubbles - A review. *Journal of Astronomy and Space Sciences*, 32(1), 13–19. <https://doi.org/10.5140/jass.2015.32.1.13>
- Kim, V. P., & Hegai, V. V. (2016). Low latitude plasma blobs: A review. *Journal of Astronomy and Space Sciences*, 33(1), 13–19. <https://doi.org/10.5140/JASS.2016.33.1.13>
- Lei, J., Zhu, Q., Wang, W., Burns, A. G., Zhao, B., Luan, X., et al. (2015). Response of the topside and bottomside ionosphere at low and middle latitudes to the October 2003 superstorms. *Journal of Geophysical Research: Space Physics*, 120(8), 6974–6986. <https://doi.org/10.1002/2015JA021310>
- Li, J., Chen, Y., Liu, L., Le, H., Zhang, R., Huang, H., & Li, W. (2021). Occurrence of ionospheric equatorial ionization anomaly at 840 km height observed by the DMSP satellites at solar maximum dusk. *Space Weather*, 19(5), e2020SW002690. <https://doi.org/10.1029/2020SW002690>
- Lin, C. H., Hsiao, C. C., Liu, J. Y., & Liu, C. H. (2007). Longitudinal structure of the equatorial ionosphere: Time evolution of the four-peaked EIA structure. *Journal of Geophysical Research: Space Physics*, 112(A12), A12305. <https://doi.org/10.1029/2007JA012455>

- Lin, C. H., Liu, J. Y., Fang, T. W., Chang, P. Y., Tsai, H. F., Chen, C. H., & Hsiao, C. C. (2007). Motions of the equatorial ionization anomaly crests imaged by FORMOSAT-3/COSMIC. *Geophysical Research Letters*, *34*(19), L19101. <https://doi.org/10.1029/2007GL030741>
- Lin, C. S., Sutton, E. K., Wang, W., Cai, X., Liu, G., Henney, C. J., & Cooke, D. L. (2022). Satellite in situ electron density observations of the midlatitude storm enhanced density on the noon meridional plane in the F region during the 20 November 2003 magnetic storm. *Journal of Geophysical Research: Space Physics*, *127*(5), e2021JA029831. <https://doi.org/10.1029/2021JA029831>
- Liu, J., Zhang, D., Mo, X., Xiong, C., Hao, Y., & Xiao, Z. (2020). Morphological differences of the northern equatorial ionization anomaly between the eastern Asian and American sectors. *Journal of Geophysical Research: Space Physics*, *125*(3), e2019JA027506. <https://doi.org/10.1029/2019JA027506>
- Liu, J. Y., Yang, W. H., Lin, C. H., Chen, Y. I., & Lee, I. T. (2013). A statistical study on the characteristics of ionospheric storms in the equatorial ionization anomaly region: GPS-TEC observed over Taiwan. *Journal of Geophysical Research: Space Physics*, *118*(6), 3856–3865. <https://doi.org/10.1002/jgra.50366>
- Liu, L., Wan, W., Ning, B., Pirog, O. M., & Kurki, V. I. (2006). Solar activity variations of the ionospheric peak electron density. *Journal of Geophysical Research*, *111*(A8), A08304. <https://doi.org/10.1029/2006JA011598>
- Loutfi, A., Pitout, F., Bounhir, A., Benkhalidoun, Z., Makela, J. J., Abamni, S., et al. (2022). Interhemispheric asymmetry of the equatorial ionization anomaly (EIA) on the African sector over 3 years (2014–2016): Effects of thermospheric meridional winds. *Journal of Geophysical Research: Space Physics*, *127*(9), e2021JA029902. <https://doi.org/10.1029/2021JA029902>
- Luan, X. (2021). Equatorial ionization anomaly variations during geomagnetic storms. In G. Huang, G. Lu, Y. Zhang, & L. J. Paxton (Eds.), *Ionosphere dynamics and applications*. <https://doi.org/10.1002/9781119815617.ch13>
- Luan, X., Wang, P., Dou, X., & Liu, Y. C.-M. (2015). Interhemispheric asymmetry of the equatorial ionization anomaly in solstices observed by COSMIC during 2007–2012. *Journal of Geophysical Research: Space Physics*, *120*(4), 3059–3073. <https://doi.org/10.1002/2014ja020820>
- Mannucci, A. J., Tsurutani, B. T., Iijima, B. A., Komjathy, A., Saito, A., Gonzalez, W. D., et al. (2005). Dayside global ionospheric response to the major interplanetary events of October 29–30, 2003 “Halloween storms”. *Geophysical Research Letters*, *32*(12), L12S02. <https://doi.org/10.1029/2004GL021467>
- Mannucci, A. J., Wilson, B. D., Yuan, D. N., Ho, C. H., Lindqwister, U. J., & Runge, T. F. (1998). A global mapping technique for GPS-derived ionospheric total electron content measurements. *Radio Science*, *33*(3), 565–582. <https://doi.org/10.1029/97rs02707>
- Maruyama, N., Sun, Y.-Y., Richards, P. G., Middlecoff, J., Fang, T.-W., Fuller-Rowell, T. J., et al. (2016). A new source of the midlatitude ionospheric peak density structure revealed by a new ionosphere-plasmasphere model. *Geophysical Research Letters*, *43*(6), 2429–2435. <https://doi.org/10.1002/2015GL067312>
- McClure, J. P., Hanson, W. B., & Hoffman, J. H. (1977). Plasma bubbles and irregularities in the equatorial ionosphere. *Journal of Geophysical Research*, *82*(19), 2650–2656. <https://doi.org/10.1029/ja082i019p02650>
- Mendillo, M. (2006). Storms in the ionosphere: Patterns and processes for total electron content. *Reviews of Geophysics*, *44*(4), RG4001. <https://doi.org/10.1029/2005RG000193>
- Mendillo, M., Huang, C., Pi, X., Rishbeth, H., & Meier, R. (2005). The global ionospheric asymmetry in total electron content. *Journal of Atmospheric and Solar-Terrestrial Physics*, *67*(15), 1377–1387. <https://doi.org/10.1016/j.jastp.2005.06.021>
- Meng, X., & Verkhoglyadova, O. P. (2023). Total electron content intensification dataset for years 2003 to 2022 [Dataset]. JPL Open Repository. <https://doi.org/10.48577/jpl.KXY5BW>
- Muldrew, D. B. (1965). F-layer ionization troughs deduced from Alouette data. *Journal of Geophysical Research*, *70*(11), 2635–2650. <https://doi.org/10.1029/jz070i011p02635>
- Namba, S., & Maeda, K.-I. (1939). *Radio wave propagation*. Corona Publishing.
- Nigusse, M., Jakowski, N., & Hoque, M. (2022). Characterization and climatological modeling of equatorial ionization anomaly (EIA) crest position. *Journal of Geophysical Research: Space Physics*, *127*(12), e2022JA030798. <https://doi.org/10.1029/2022JA030798>
- Oya, H., Takahashi, T., & Watanabe, S. (1986). Observation of low latitude ionosphere by the impedance probe on board the Hinotori satellite. *Journal of Geomagnetism and Geoelectricity*, *38*(2), 111–123. <https://doi.org/10.5636/jgg.38.111>
- Padatella, N. M., & Forbes, J. M. (2010). Global structure of the lunar tide in ionospheric total electron content. *Geophysical Research Letters*, *37*(6), L06103. <https://doi.org/10.1029/2010GL042781>
- Qian, L., Burns, A. G., Solomon, S. C., & Wang, W. (2013). Annual/semi-annual variation of the ionosphere. *Geophysical Research Letters*, *40*(10), 1928–1933. <https://doi.org/10.1002/grl.50448>
- Rajesh, P. K., Liu, J. Y., Balan, N., Lin, C. H., Sun, Y. Y., & Pulinets, S. A. (2016). Morphology of midlatitude electron density enhancement using total electron content measurements. *Journal of Geophysical Research: Space Physics*, *121*(2), 1503–1517. <https://doi.org/10.1002/2015JA022251>
- Rishbeth, H. (1998). How the thermospheric circulation affects the ionospheric F2-layer. *Journal of Atmospheric and Solar-Terrestrial Physics*, *60*(14), 1385–1402. [https://doi.org/10.1016/s1364-6826\(98\)00062-5](https://doi.org/10.1016/s1364-6826(98)00062-5)
- Rishbeth, H., & Mendillo, M. (2001). Patterns of F2-layer variability. *Journal of Atmospheric and Solar-Terrestrial Physics*, *63*(15), 1661–1680. [https://doi.org/10.1016/s1364-6826\(01\)00036-0](https://doi.org/10.1016/s1364-6826(01)00036-0)
- Roma-Dollase, D., Hernandez-Pajares, M., Krankowski, A., Kotulak, K., Ghoddousi-Fard, R., Yuan, Y., et al. (2018). Consistency of seven different GNSS global ionospheric mapping techniques during one solar cycle. *Journal of Geodesy*, *92*(6), 691–706. <https://doi.org/10.1007/s00190-017-1088-9>
- Sagawa, E., Immel, T. J., Fre, H. U., & Mende, S. B. (2005). Longitudinal structure of the equatorial anomaly in the nighttime ionosphere observed by IMAGE/FUV. *Journal of Geophysical Research*, *110*(A11), A11302. <https://doi.org/10.1029/2004JA010848>
- Sato, T. (1959). Morphology of ionospheric F2 disturbances in the polar regions. *Report of Ionosphere and Space Research in Japan*, *13*, 91–95.
- Sparks, L., Altshuler, E., Pandya, N., Blanch, J., & Walter, T. (2021). WAAS and the ionosphere - A historical perspective: Monitoring storms. *Navigation: Journal of the Institute of Navigation*, *69*(1), 503. <https://doi.org/10.33012/navi.503>
- Starr, G., Mrak, S., Nishimura, Y., Hirsch, M., Ishwar, P., & Semeter, J. (2022). Automatic identification of the main ionospheric trough in total electron content images. *Space Weather*, *24*(6), e2021SW002994. <https://doi.org/10.1029/2021SW002994>
- Sun, H., Chen, Y., Zou, S., Ren, J., Chang, Y., Wang, Z., & Coster, A. (2023). Complete global total electron content map database based on a video imputation algorithm VISTA. *Scientific Data*, *10*(1), 236. <https://doi.org/10.1038/s41597-023-02138-7>
- Torr, M. R., & Torr, D. G. (1973). The seasonal behavior of the f2 layer of the ionosphere. *Journal of Atmospheric and Solar-Terrestrial Physics*, *35*(12), 2237–2251. [https://doi.org/10.1016/0021-9169\(73\)90140-2](https://doi.org/10.1016/0021-9169(73)90140-2)
- Tsai, H.-F., Liu, J.-Y., Tsai, W.-H., Liu, C.-H., Tseng, C.-L., & Wu, C.-C. (2001). Seasonal variations of the ionospheric total electron content in Asian equatorial anomaly regions. *Geophysical Research Letters*, *106*(A12), 30363–30369. <https://doi.org/10.1029/2001ja001107>

- Tsai, T. C., Jhuang, H. K., Lee, L. C., & Ho, Y. Y. (2019). Ionospheric peaked structures and their local time, seasonal, and solar activity dependence based on global ionosphere maps. *Journal of Geophysical Research: Space Physics*, *124*(10), 7994–8014. <https://doi.org/10.1029/2019JA026899>
- Tulasi Ram, S., Su, S.-Y., & Liu, C. H. (2009). FORMOSAT-3/COSMIC observations of seasonal and longitudinal variations of equatorial ionization anomaly and its interhemispheric asymmetry during the solar minimum period. *Journal of Geophysical Research*, *114*(A6), A06311. <https://doi.org/10.1029/2008JA013880>
- Verkhoglyadova, O., Maus, N., & Meng, X. (2021). Classification of high density regions in global ionospheric maps with neural networks. *Earth and Space Science*, *8*(7), e2021EA001639. <https://doi.org/10.1029/2021EA001639>
- Verkhoglyadova, O., Meng, X., & Kosberg, J. (2022). Understanding large-scale structure in global ionospheric maps with visual and statistical analyses. *Frontiers in Astronomy and Space Sciences*, *9*, 852222. <https://doi.org/10.3389/fspas.2022.852222>
- Walker, G. O. (1981). Longitudinal structure of the F-region equatorial anomaly—A review. *Journal of Atmospheric and Solar-Terrestrial Physics*, *43*(8), 763–774. [https://doi.org/10.1016/0021-9169\(81\)90052-0](https://doi.org/10.1016/0021-9169(81)90052-0)
- Wu, T.-Y., Liu, J.-Y., Lin, C.-Y., & Chang, L. C. (2020). Response of ionospheric equatorial ionization crests to lunar phase. *Geophysical Research Letters*, *47*(7), e2019GL086862. <https://doi.org/10.1029/2019GL086862>
- Xiong, C., Luhr, H., Sun, L., Luo, W., Park, J., & Hong, Y. (2019). Long-lasting latitudinal four-peak structure in the nighttime ionosphere observed by the Swarm constellation. *Journal of Geophysical Research: Space Physics*, *124*(11), 9335–9347. <https://doi.org/10.1029/2019JA027096>
- Yeh, K. C., Franke, S. J., Andreeva, E. S., & Kunitsyn, V. E. (2001). An investigation of motions of the equatorial anomaly crest. *Geophysical Research Letters*, *28*(24), 4517–4520. <https://doi.org/10.1029/2001gl013897>
- Yonezawa, T. (1959). On the seasonal and non-seasonal annual variations and semi-annual variations in the noon and midnight densities of the F2 layer in middle latitudes. *Journal of the Radio Research Laboratory (Japan)*, *6*, 651.
- Yue, X., Schreiner, W. S., Kuo, Y.-H., & Lei, J. (2015). Ionosphere equatorial ionization anomaly observed by GPS radio occultations during 2006–2014. *Journal of Atmospheric and Solar-Terrestrial Physics*, *129*, 30–40. <https://doi.org/10.1016/j.jastp.2015.04.004>
- Zeng, Z., Burns, A., Wang, W., Lei, J., Solomon, S., Syndergaard, S., et al. (2008). Ionospheric annual asymmetry observed by the COSMIC radio occultation measurements and simulated by the TIEGCM. *Journal of Geophysical Research*, *113*(A7), A07305. <https://doi.org/10.1029/2007JA012897>